PHYSICAL REVIEW B **77**, 184107 (2008)

Multiple elastic scattering of core-loss electrons in atomic resolution imaging

C. Dwyer*
Monash Centre for Electron Microscopy, Monash University, Victoria 3800, Australia
and Department of Materials Engineering, Monash University, Victoria 3800, Australia

S. D. Findlay and L. J. Allen
School of Physics, University of Melbourne, Victoria 3010, Australia

(Received 18 February 2008; revised manuscript received 14 April 2008; published 9 May 2008)

We consider the elastic scattering of a fast incident electron both prior and subsequent to its involvement in an atomic inner-shell ionization (core-loss) event in a crystal. By using numerical simulations, it is shown that elastic scattering subsequent to ionization can strongly affect the qualitative features of atomic resolution core-loss images of crystals recorded in the scanning transmission electron microscope (STEM). This conclusion holds even for a thin crystal foil and for a relatively large detector, which is matched to the probe-forming aperture in an aberration-corrected STEM. Such a conclusion is potentially very important for the interpretation of experimental core-loss images. We also introduce an approximate model that incorporates the effects of elastic scattering subsequent to ionization in the case of a small detector.

DOI: 10.1103/PhysRevB.77.184107 PACS number(s): 61.05.jd, 61.85.+p, 68.37.Ma, 79.20.Uv

I. INTRODUCTION

While the theory describing the inelastic scattering of fast electrons in crystals dates back half a century,[1–15] the complexity of the theory is such that very few analytic solutions are possible[16] and the conclusions that may be drawn from a study of the equations themselves are limited. The full range of behavior, subtleties, and nuances can only be revealed through detailed numerical simulations. The scope of early numerical simulations, despite providing many insights that have led to our understanding of imaging in the electron microscope,[4,5,17–19] was limited by the computing resources available. Through the steady advance in computing power, the past decade or so has seen many successes in the elaborate calculation of inelastic scattering in electron microscopy,[11–15,20–23] although the underlying principles on which these calculations are based have been largely understood for much longer.

Given the limitations of available computing power, progress has relied on making good approximations that simplify the general theory to a more tractable form. One such is the so-called single inelastic scattering approximation, which assumes that no electrons that have undergone some particular energy loss will undergo any further energy loss.[1,8] This is agreed to be a good approximation for atomic inner-shell ionization (core-loss scattering), although it is of limited applicability to thermal and plasmon scattering. Another simplifying approximation is to assume that subsequent to inelastic scattering, the electrons no longer feel the crystal potential and can therefore be described by plane waves.[1,9,24] This is never true in detail but is taken to give a reasonable representation of the total signal obtained when integrating over a moderate collection angle, the argument being that if the subsequent elastic scattering perturbs the intensity distribution on a scale smaller than that of the detector, then the error introduced by omitting this scattering is small. This is often referred to as a single channeling approximation because the electron is allowed to elastically scatter or channel prior to the ionization event but not subsequent to it. Allowing for elastic scattering both prior and subsequent to the inelastic event is then referred to as double channeling.

In his seminal 1957 paper, Yoshioka[1] neglected all inelastic transitions not involving the crystal ground state. Among other things, this prevents elastic scattering within an excited state, implying the single channeling approximation. This was noted by Howie[2] and rectified by him in that work and others in subsequent works.[3,5–9] Double channeling calculations incorporating a small number of Bloch waves were performed by Rez *et al.*[4] A decade ago, Josefsson and Allen[12] showed, by comparison with full double channeling calculations, that the single channeling approximation sufficed to simulate the orientation dependence of the aluminum K-shell electron energy loss spectroscopy (EELS) signal resulting from a 120 keV plane wave incident on an aluminum crystal in systematic row orientation, provided that the detector semiangle was around 20 mrad or larger. Despite the fact that aluminum is a relatively weak scatterer and the scattering in systematic row orientations is generally weaker than that in zone axis orientations, this result has been taken as license to use the single channeling approximation in much subsequent work, even when the detector size is of the order of 10 mrad (on the other hand, see Ref. 14, where double channeling was shown to give better agreement with the experiment).

Advances in computing power mean that it is now possible to check how well such "standard assumptions" hold up. Moreover, advances in scanning transmission electron microscope (STEM) instrumentation make it important to do so. As the sensitivity of experiments now approaches the single atom level, and with simulations playing an increasing role in obtaining the maximum amount of information from the experimental data, it is vital to establish the limitations of the approximations invoked in the analysis. In this paper, we explore the extent to which the single channeling approximation is valid for core-loss events in the STEM, both qualitatively, as regards the shape of core-loss images, and quantitatively.

©2008 The American Physical Society

II. THEORY

Let us adopt the single inelastic scattering approximation. It has been shown that the inelastic scattering resulting from the inner-shell ionization of different atoms may be incoherently treated.[25,26] Furthermore, the ejected atomic electron can have a number of different final states. We account for this by modeling the transition from the elastic wave function ψ_0 incident upon atom α to the inelastic wave function ψ_n^α resulting when a core electron of atom α has been ejected into some state, which we characterize by the set of quantum numbers denoted by n. The basis of our approach is the following equation:[27]

$$\psi_n^\alpha(\mathbf{r}) = -i\sigma_n V_{n0}^\alpha(\mathbf{r})\psi_0(\mathbf{r}), \tag{1}$$

where $\sigma_n = \gamma m/2\pi\hbar^2 k_n$ is the interaction constant for the fast electron after energy loss and

$$V_{n0}^\alpha(\mathbf{r}) = \int_{-\infty}^{\infty} \mathrm{d}z V_{n0}^\alpha(\mathbf{r},z)e^{2\pi i q_z z}, \tag{2}$$

in which $V_{n0}(\mathbf{r},z)$ is a matrix element of the type $V_{nm}(\mathbf{r},z) = \langle n|V_{\mathrm{int}}|m\rangle$, $q_z \approx k_0\Delta E/2E_0$, and V_{int} is the pairwise Coulomb interaction between the incident fast electron and all the particles in the crystal. The crystal states $|m\rangle$ and $|n\rangle$ will generally be approximated as single electron wave functions with the assumption that the ejection of the atomic electron during ionization is the only significant change to the state of the crystal.

Incorporating channeling prior to the inelastic scattering event means including dynamical elastic scattering in calculating ψ_0 at the depth of the inelastic interaction. Incorporating channeling subsequent to the inelastic scattering event means including dynamical elastic scattering in propagating ψ_n^α from the depth of the inelastic interaction to the exit face of the crystal. The latter is the crux of double channeling theory. For a crystal of thickness t, and adopting the projection approximation for simplicity (i.e., neglecting higher-order Laue zone effects), such ideas are neatly represented by using propagator theory,[28]

$$\psi_n^\alpha(\mathbf{r},t) = \int d^2\mathbf{r}_2 iG_{nn}(\mathbf{r},\mathbf{r}_2,t-z_\alpha)(-i\sigma_n)V_{n0}^\alpha(\mathbf{r}_2) \times \int d^2\mathbf{r}_1 iG_{00}(\mathbf{r}_2,\mathbf{r}_1,z_\alpha)\psi_0(\mathbf{r}_1), \tag{3}$$

where $\psi_0(\mathbf{r}) \equiv \psi_0(\mathbf{r},0)$ is the elastic wave function at the entrance surface and G_{00} and G_{nn} are propagators for elastic scattering prior and subsequent to the inelastic interaction, respectively. The multislice method[29,30] provides a clear and routine way of carrying out both propagations.

Alternatively, the same idea can be described in the following reciprocal space form:

$$\Psi_n^\alpha(\mathbf{g},t) = \sum_{\mathbf{g}_3} \mathcal{S}_{nn}(\mathbf{g},\mathbf{g}_3,t-z_\alpha)\sum_{\mathbf{g}_2}(-i\sigma_n)\widetilde{V}_{n0}^\alpha(\mathbf{g}_3-\mathbf{g}_2) \times \sum_{\mathbf{g}_1}\mathcal{S}_{00}(\mathbf{g}_2,\mathbf{g}_1,z_\alpha)\Psi_0(\mathbf{g}_1), \tag{4}$$

where $\Psi_0(\mathbf{g}) \equiv \Psi_0(\mathbf{g},0)$ is the reciprocal space form of the elastic wave function at the entrance surface, the $\mathbf{g}$'s denote reciprocal space vectors on some mesh, which may be finer than the reciprocal space lattice (which, in principle, should be continuous but for numerical implementation will be discrete, hence our notation), $\widetilde{V}_{n0}^\alpha$ is the two-dimensional Fourier transform of the projected transition matrix element defined above, and $\mathcal{S}_{00}$ and $\mathcal{S}_{nn}$ are essentially the scattering matrices introduced by Sturkey,[31] with subscripts here indicating the energy dependence.

Equation (4) and, upon Fourier transform, Eq. (3) give the complex amplitude in the diffraction pattern resulting from the inelastic transition of a single atom to a single final state. To simulate the total intensity in the diffraction pattern at a given energy loss requires the sum of intensities of all contributing final states from all contributing atoms in the sample (or rather all significant contributing final states, which tends to be only a modest number for energy losses near the ionization edge[27]). For thicker crystals, this requires significant computing power. The multislice version [Eq. (3)] will scale as the square of the thickness since the number of atoms and the number of propagating steps both linearly increase with thickness. The scattering matrix version [Eq. (4)] can be evaluated via Bloch wave methods,[32–34] which makes the scaling linear with thickness—since any propagation can be accomplished in a single step—but introduces a stronger dependence on the number of beams used. When evaluated via Bloch wave methods, Eq. (4) is essentially the result of Weickenmeier and Kohl.[35]

The standard technique for incorporating the loss of coherence due to the incoherent summation over final states at the interaction site, rather than in the diffraction plane, is through the use of the mixed dynamic form factor (MDFF).[36–38] This falls out of the present approach by taking the intensity of Eq. (4), summing over final states n and exchanging the order of the summations,

$$\sum_n |\Psi_n^\alpha(\mathbf{k},t)|^2 = \sum_{\mathbf{g}_3,\mathbf{h}_3}\mathcal{S}_{nn}(\mathbf{k},\mathbf{g}_3,t-z_\alpha)\mathcal{S}_{nn}^*(\mathbf{k},\mathbf{h}_3,t-z_\alpha) \times \sum_{\mathbf{g}_2,\mathbf{h}_2}\left[\sum_n \sigma_n^2\widetilde{V}_{n0}^\alpha(\mathbf{g}_3-\mathbf{g}_2)\widetilde{V}_{n0}^{\alpha*}(\mathbf{h}_3-\mathbf{h}_2)\right] \times \sum_{\mathbf{g}_1,\mathbf{h}_1}\mathcal{S}_{00}(\mathbf{g}_2,\mathbf{g}_1,z_\alpha)\mathcal{S}_{00}^*(\mathbf{h}_2,\mathbf{h}_1,z_\alpha) \times \Psi_0(\mathbf{g}_1)\Psi_0^*(\mathbf{h}_1). \tag{5}$$

The above expression may be considered to constitute the diagonal elements of a density matrix. The term in square brackets is very closely related to the MDFF: it is the product of the MDFF and terms constituting Fourier transforms of the Coulomb interaction. The sum over atom sites in the plane z_α can be incorporated as a site term within this quantity. If the scattering matrices are evaluated via Bloch wave methods, the sum over depths (not included in the above expression) can be converted to an integral and analytically performed prior to numerical implementation (see Ref. 39 and references therein). Because the $\mathcal{S}_{nn}$ matrices have been taken outside the sum over final states, the above expression strictly applies only for a single energy loss. However, the expression can be integrated over a finite energy window and, assuming that the energy dependence of $\mathcal{S}_{nn}$ is weak on the scale of the energy window,[40] this integration can, to a good approximation, be applied to the MDFF term alone. The resultant expression in the scattering matrix notation together with these assumptions can be found in Ref. 39 and in other notations earlier in the literature (see, for instance, Ref. 14).

The gains in Eq. (5) of not having to separately propagate the inelastic wave functions resulting from different final states of each atom (and from different atoms at the same depth if a site-dependent term is included) must be weighed against the significantly increased number of summations over reciprocal space vectors. Indeed, Weickenmeier and Kohl[35] proposed the approach embodied in Eq. (4) as a much faster alternative to approaches similar to Eq. (5). The utility of the latter, and its more elaborate relations in mixed dynamical object transparency and/or density matrix models,[10,11,41] lies in the insight they provide for the balancing of coherent and incoherent effects.[42,43] They are rarely used for detailed double channeling calculations (see, however, Ref. 44).

However, the MDFF approach comes into its own if the single channeling approximation is used. In this case, the Bloch wave final states reduce to plane waves and the scattering matrices $\mathcal{S}_{nn}$ become diagonal: $\mathcal{S}_{nn}(\mathbf{g},\mathbf{g}',t-z_\alpha) = \delta_{\mathbf{g},\mathbf{g}'}\exp[-\pi i\lambda_n(t-z_\alpha)\mathbf{g}^2]$. Using this result in Eq. (5) gives

$$\sum_n |\Psi_n^\alpha(\mathbf{k},t)|^2 = \sum_{\mathbf{g},\mathbf{h}}\left[\sum_n \sigma_n^2 \tilde{V}_{n0}^\alpha(\mathbf{k}-\mathbf{g})\tilde{V}_{n0}^{\alpha*}(\mathbf{k}-\mathbf{h})\right] \times \Psi_0(\mathbf{g},z_\alpha)\Psi_0^*(\mathbf{h},z_\alpha), \tag{6}$$

which may be recast into the following real space form:

$$\sum_n |\Psi_n^\alpha(\mathbf{k},t)|^2 = \int\int d^2\mathbf{r}d^2\mathbf{r}' \times\left[\sum_n \sigma_n^2 V_{n0}^\alpha(\mathbf{r}')V_{n0}^{\alpha*}(\mathbf{r})e^{2\pi i\mathbf{k}\cdot(\mathbf{r}-\mathbf{r}')}\right] \times \psi_0(\mathbf{r}',z_\alpha)\psi_0^*(\mathbf{r},z_\alpha). \tag{7}$$

The signal recorded in an experiment will be the integral of this intensity over the portion of the diffraction plane taken up by the detector and summing over all contributing atoms,

$$\begin{aligned} I &= \sum_{\mathbf{k}} \tilde{D}(\mathbf{k})\sum_{\alpha,n}|\Psi_n^\alpha(\mathbf{k},t)|^2 \\ &= \sum_\alpha \int\int d^2\mathbf{r}d^2\mathbf{r}'\left[\sum_n \sigma_n^2 V_{n0}^\alpha(\mathbf{r}')V_{n0}^{\alpha*}(\mathbf{r})\sum_{\mathbf{k}}\tilde{D}(\mathbf{k})e^{2\pi i\mathbf{k}\cdot(\mathbf{r}-\mathbf{r}')}\right] \\ &\quad\times\psi_0(\mathbf{r}',z_\alpha)\psi_0^*(\mathbf{r},z_\alpha), \end{aligned} \tag{8}$$

where $\tilde{D}$ equals unity (zero) for points lying on (off) the detector. Assuming a periodic specimen, we can form an effective scattering potential for all the atoms in the plane z_α, which embodies the detector geometry from the bracketed term, and convert the sum over slices into an integral along the z axis, giving the following general form:

$$I = \int_0^t dz\int d^2\mathbf{r}\int d^2\mathbf{r}'\,\psi_0^*(\mathbf{r},z)W_{\text{eff}}(\mathbf{r},\mathbf{r}')\psi_0(\mathbf{r}',z). \tag{9}$$

Should it transpire that $W_{\text{eff}}(\mathbf{r},\mathbf{r}') \approx V_{\text{eff}}(\mathbf{r})\delta(\mathbf{r}-\mathbf{r}')$, as is the case provided that the detector collection angle is sufficiently large,[27,39,45] which is usually true for thermal diffuse scattering experiments and sometimes true for inner-shell ionization, this expression reduces to

$$I = \int_0^t dz\int d^2\mathbf{r}|\psi_0(\mathbf{r},z)|^2 V_{\text{eff}}(\mathbf{r}), \tag{10}$$

which is often referred to as the incoherent imaging or object function model. The efficiency of such models for computation and the direct interpretability of Eq. (10) makes this an attractive regime in which to work.

In Sec. III, we explore the validity of the single channeling approximation by direct comparison to the double channeling approach based on Eqs. (2) and (3). The propagations in Eq. (3) were calculated by using the multislice method. Given the computational demand of double channeling calculations, we concentrate on exploring the dependence of double channeling on only two parameters: detector geometry and specimen thickness. We anticipate these to be more important than, say, such quantities as the probe energy and the ionization edge. The scattering strength of the specimen is obviously important; we will use $\mathrm{SrTiO_3}$ for our case study, which is a technologically relevant material of moderate scattering strength.

III. SIMULATIONS

Before presenting the results of our comparison, let us first explore, in the context of STEM EELS, the role of channeling subsequent to the ionization event. For this purpose, consider the Ti L_{23} energy spectroscopic diffraction pattern of $\mathrm{SrTiO_3}$ viewed along the $\langle 001\rangle$ direction. This particular ionization edge was chosen for its experimental accessibility, while the crystal structure was chosen for its relative simplicity in addition to its continuing technological interest. An aberration-free 100 keV electron probe with a 25 mrad convergence semiangle (modeling that produced in a state-of-the-art STEM) was used in a multislice approach following from Eqs. (2) and (3). Thermal absorption was included in the channeling prior and subsequent to ionization following the approach of Ref. 46. An isolated atom model was adopted to describe the ionization events. The initial (bound) state of the atomic electron was calculated by using a Hartree–Slater model.[47] The states of the ejected atomic electron were determined from the Herman–Skillman potential by using an angular momentum basis, as described in Ref. 27. This approach neglects the influence of the crystal potential on the state of the ejected atomic electron. Although such effects alter the probability for the inelastic scattering event, which gives rise to fine structure in the energy loss spectrum, their influence on the distribution of inelastically scattered electrons is expected to be minor. Furthermore, since the present work is primarily concerned with the *differences* between the single and double channeling results, such fine

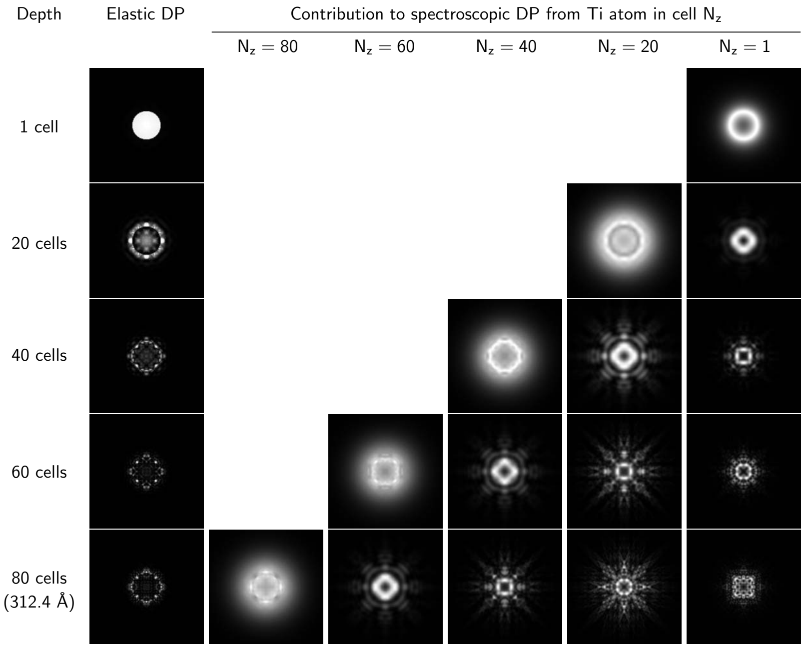

FIG. 1. Contributions to spectroscopic diffraction patterns (DP) for different thicknesses at an energy loss of 10 eV above the Ti L_{23} ionization edge generated by a probe atop the Ti-O column in $\langle 001 \rangle$ SrTiO$_3$. The leftmost column shows the elastic diffraction pattern from a sample of the thickness given to the left of each image. The remaining columns show reciprocal space intensities of an inelastic fast electron wave function resulting from the ionization of a Ti atom at the depth given above the column. Different rows give the reciprocal space intensity of these inelastic wave functions at different depths, having further elastically scattered from the depth at which they were produced (double channeling). The intensities in any row constitute contributions to the energy spectroscopic DP from a sample of that thickness. Each pattern shows the scattering within ±100 mrad.

structure effects can be neglected. The present calculation includes ejected atomic electron states with orbital angular momentum quantum numbers $l'=0$, 1, and 2. With the probe directly positioned above the Ti-O column, Fig. 1 shows the contributions that various Ti atoms in that column make to the spectroscopic diffraction pattern at 10 eV above the Ti L_{23} edge. The different columns correspond to an inelastic final state resulting from the ionization of a Ti atom at the depth given above the column, in units of cell number. The rows correspond to the depth, in cell number, at which the reciprocal space intensity of this inelastic wave function is plotted. This quantity would contribute to the diffraction pattern if this depth were the exit face of the crystal, so the energy spectroscopic diffraction pattern for a given crystal thickness is obtained from adding the intensities, along with others not shown, across the appropriate row (excluding the leftmost column entry, which is the elastic diffraction pattern at this depth). With increasing depth, channeling subsequent to ionization causes the contribution from a given atom to contain features of increasingly fine detail. On the other hand, the contributions from different atoms that have channeled over equal depths show a remarkable qualitative similarity.

The top pattern in each of the five rightmost columns in Fig. 1 represents the single channeling result for a crystal thickness of 80 unit cells (about 300 Å), i.e., the summation of these patterns (and patterns from the other Ti atoms which are not shown) yields the spectroscopic diffraction pattern that would be formed if the incident electron did not undergo channeling subsequent to ionization. Analogously, the bottom pattern in each of the five rightmost columns represents the double channeling result for a crystal thickness of 80 unit cells. Clearly, the single channeling approximation is completely inadequate for describing the spectroscopic diffraction pattern for a crystal of such thickness.

However, in typical STEM EELS experiments at high spatial resolution, the full spectroscopic diffraction pattern is not recorded but rather only the total signal within some circular on-axis detector. To this end, and given that the contribution from the topmost Ti atom ($N_z=1$ in Fig. 1) is presumably most influenced by channeling subsequent to ionization, Fig. 2(a) shows the integrated signal from this atom as a function of specimen depth and detector aperture semiangle. Despite the differences seen in this atom's contribution to the spectroscopic diffraction pattern at different depths in Fig. 1, the integrated signal seems to be very similar for depths in the range of 20–80 unit cells. Apart from thermal absorption subsequent to ionization causing an overall decrease of the signal with increasing depth, we observe only relatively minor variations out to about 20 mrad. On the other hand, the atom's contribution at a depth of one unit cell, which represents the single channeling case without thermal absorption subsequent to ionization, gives a noticeably lower signal for semiangles smaller than about 30 mrad. This indicates the focusing effect of channeling subsequent to ionization. For all depths, the signal becomes increasingly similar with increasing detector semiangle and eventually saturates as the detector size encompasses nearly all of the inelastically scattered intensity. This is most easily seen in Fig. 2(b), which compares the signal at depths of 1 cell and 80 cells, where the former is corrected for thermal absorption subsequent to ionization for a total thickness of 80 cells. This correction was made by multiplying by a factor $e^{-t/\lambda}$, where λ is the mean free path for thermal scattering, which at this zone axis was determined to be about 700 Å by using the absorptive potentials described in Ref. 46. The corrected signal at a depth of 1 unit cell represents the single channeling result for a total thickness of 80 cells. Ideally, the curves in Fig. 2(b) should exactly coincide at large semiangles, where the effects of channeling subsequent to ionization are integrated out. The observed discrepancy arises because channeling subsequent to ionization affects the degree of thermal absorption, an effect not treated in our single channeling approximation. However, as will be shown, the differences be-

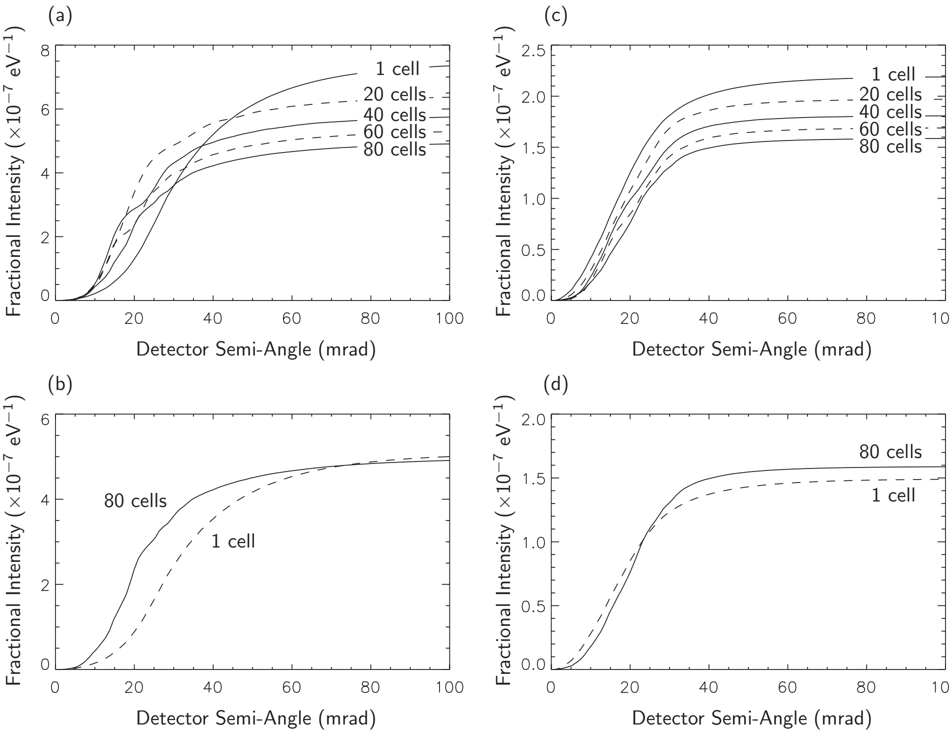

FIG. 2. (a) The integrated Ti L_{23} signal from the topmost Ti atom considered in Fig. 1 as a function of specimen depth and detector semiangle. (b) The signal at depths of 1 cell and 80 cells, the former being corrected for absorption due to thermal scattering for a thickness of 80 cells. Data analogous to (a) and (b) but for a probe displaced 0.78 Å along the ⟨100⟩ direction from the Ti-O column are plotted in (c) and (d).

tween the single and double channeling calculations are typically significantly larger than the error arising from this effect, and so our conclusions are unaffected.

So far, only a single probe position directly above the Ti-O column has been considered. However, this alone only indicates quantitative deviations in the detected signal, and such quantitative analysis is beyond the ability of routine experiments. Much more pertinent to STEM EELS images obtained at high spatial resolution is the variation in shape of the detected signal as the probe is shifted. To this end, Figs. 2(c) and 2(d) show the integrated signal analogous to Figs. 2(a) and 2(b) but with the probe displaced 0.78 Å along the ⟨100⟩ direction from the Ti-O column. Both the total signal and the relative magnitude of fluctuations with changing depth and constant detector semiangle are smaller than when the probe was centered on the Ti-O column (the former result is expected for a probe displaced from the center of the interaction region). Most importantly though, the single channeling approximation gives results very similar to the signal at a depth of 80 cells [Fig. 2(d)], whereas it predicted significantly lower intensity for semiangles less than about 30 mrad when the probe was on the Ti-O column [Fig. 2(b)]. This implies that channeling subsequent to ionization will cause a change in the shape or at least in the width of the core-loss image that could be detected with current instrumentation.

The effect of double channeling on the contribution from a single atom at the crystal entrance surface is, in a sense, the worst-case result because the contribution from such an atom channels over the greatest distance. For an atom near the exit surface, double channeling will not be very important. Still, for a probe focused at the entrance surface, the strength of the contributions from atoms near the entrance surface is expected to be the largest since the probe has not been dispersed by scattering and absorption within the crystal. Hence, on these grounds and given the results in Figs. 2(b) and 2(d), we might expect double channeling to have a significant effect on the core-loss image.

In Fig. 3, we compare single and double channeling calculations of the core-loss image generated by a focused electron probe as it scans across $SrTiO_3$. The computational demand of double channeling calculations means that we are unfortunately restricted to calculations where the electron probe moves along only one dimension, i.e., a "line scan." Nonetheless, the significance of double channeling effects as a function of the various experimental parameters can be readily gauged from such calculations. Moreover, most high spatial resolution EELS experiments reported to date have involved a similar restriction, though for entirely different (experimental) reasons (see, however, Refs. 48–50). In an effort to the reduce the computational demands of the double channeling calculations even further, the results in Fig. 3 incorporate only those excited atomic states making the greatest contribution to 95% of the total inelastic intensity. Because the majority of excited states do not give rise to a significant contribution, this significantly reduced the computation time. This approximation was tested for a number of cases, and in all cases, we found that the shape of the core-loss image was not significantly affected. Although this approximation does lead to a slight reduction of the overall strength of the core-loss signal, such quantitative deviations are beyond the ability of routine experiments, as mentioned above.

Figures 3(a)–3(c) compare, for three detector sizes, single and double channeling simulations of the O *K* loss image at 10 eV above threshold generated by a probe moving along the ⟨100⟩ direction of ⟨001⟩-oriented $SrTiO_3$. This particular ionization edge was chosen for its experimental accessibility and its relative ease of computation (*s*-state excitations involve the smallest number of important transitions for energy

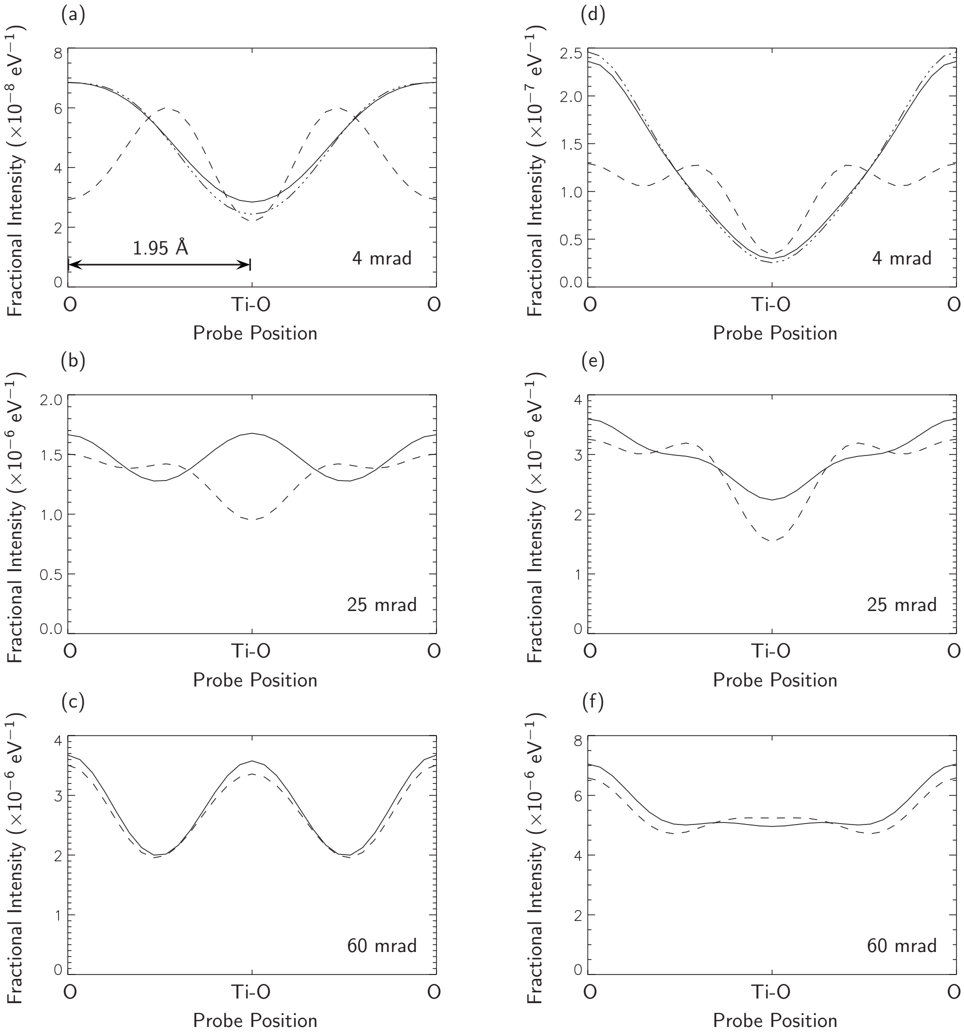

FIG. 3. Single channeling (dashed lines) and double channeling (solid lines) simulations of the O K loss image of $\langle 001 \rangle$ SrTiO$_3$ at 10 eV above threshold. The beam energy is 100 keV and the convergence semiangle is 25 mrad. The specimen thickness in (a)–(c) is 25 unit cells (about 100 Å), and in (d)–(f) is 70 unit cells (about 275 Å). Detector semiangles are indicated. Probe positions at left and right correspond to pure O atomic columns, and center corresponds to the Ti-O column. Scale bar is featured in (a). Results of an approximate double channeling model (dashed-dotted lines) are presented in (a) and (d).

losses near threshold). The crystal thickness in this case is 25 unit cells (about 100 Å). The beam energy, lens aberrations, and convergence semiangle are as before. The detector semiangles (4, 25, and 60 mrad) were chosen to be significantly smaller than, equal to, and significantly larger than the probe convergence semiangle. (The graph for the 4 mrad detector semiangle also features results of an approximate double channeling model to be discussed below.) Figures 3(d)–3(f) show analogous data for a crystal thickness of 70 unit cells (about 275 Å). As before, the single channeling calculations include a correction for thermal absorption subsequent to ionization.

From Fig. 3, it is seen that the single and double channeling predictions of the core-loss image can *qualitatively* differ for detector semiangles of 4 and 25 mrad. For example, for a thickness of 25 unit cells and a detector semiangle of 4 mrad [Fig. 3(a)], the single channeling approximation predicts maxima occurring approximately halfway between the Ti-O and O atomic columns. Such maxima correspond to the "volcano" structures often observed in single channeling calculations, where the detector semiangle is smaller than the convergence semiangle.[36,51–54] In stark contrast, the double channeling calculation places maxima on the O columns and minima on the Ti-O columns. For the 25 mrad detector [Figs. 3(b) and 3(e)], the magnitudes of the differences between the single and double channeling results tend to be smaller than for the 4 mrad detector, but qualitative differences persist. The results for the 60 mrad detector [Figs. 3(c) and 3(f)] are very similar, as expected. In fact, the small differences seen for the 60 mrad detector correspond almost entirely to the error, mentioned above, arising from the gross treatment of postionization absorption in the single channeling approximation.

In general, given the complexity of the full double channeling model and the influence of the many experimental parameters involved, it is difficult to gauge for a specific situation how the single and double channeling predictions of the core-loss image will differ, even qualitatively, without performing the full double channeling calculation. Exceptions to this observation come at the extremes of detector size. As already described, in the case where the detector is very large, the single and double channeling predictions are essentially the same, and so the simpler model may be used. In Sec. IV, it will be shown that simplifications can also be made in the case of a small detector.

IV. APPROXIMATE MODEL FOR SMALL DETECTORS

To gain some physical insight into the effects of double channeling on the core-loss image, let us introduce the following approximation, valid for small $|\mathbf{g}|$, to the postionization scattering matrix,

$$\mathcal{S}_{nn}(\mathbf{g},\mathbf{g}_1,z) \approx \mathcal{S}_{nn}(\mathbf{0},\mathbf{g}_1-\mathbf{g},z). \tag{11}$$

This approximation will be valid for a small detector with semiangle $\beta \ll d/t$, where d is the intercolumnar spacing and t is the crystal thickness. In practice, $d/t \sim 1/100$, giving $\beta \ll 10$ mrad.

Now, let us define the quantity,

$$\widetilde{W}^{\alpha}_{n0}(\mathbf{g},\mathbf{g}_1,z) = \sum_{\mathbf{g}_2} \mathcal{S}_{nn}(\mathbf{g},\mathbf{g}_2,z)\widetilde{V}^{\alpha}_{n0}(\mathbf{g}_2-\mathbf{g}_1), \tag{12}$$

which we can regard as a modified inelastic potential that incorporates the effects of double channeling. Using the above approximation to the scattering matrix,

$$\begin{aligned}\widetilde{W}^{\alpha}_{n0}(\mathbf{g},\mathbf{g}_1,z) &\approx \sum_{\mathbf{g}_2} \mathcal{S}_{nn}(\mathbf{0},\mathbf{g}_2-\mathbf{g},z)\widetilde{V}^{\alpha}_{n0}(\mathbf{g}_2-\mathbf{g}_1)\\ &= \sum_{\mathbf{g}'} \mathcal{S}_{nn}(\mathbf{0},\mathbf{g}',z)\widetilde{V}^{\alpha}_{n0}(\mathbf{g}'+\mathbf{g}-\mathbf{g}_1),\end{aligned} \tag{13}$$

so that

$$\begin{aligned}\widetilde{W}^{\alpha}_{n0}(\mathbf{g},\mathbf{g}_1,z) &\approx \widetilde{W}^{\alpha}_{n0}(\mathbf{g}-\mathbf{g}_1,z)\\ &\equiv \sum_{\mathbf{g}'} \mathcal{S}_{nn}(\mathbf{0},\mathbf{g}',z)\widetilde{V}^{\alpha}_{n0}(\mathbf{g}'+\mathbf{g}-\mathbf{g}_1).\end{aligned} \tag{14}$$

This approximation leads to a considerable simplification: adopting this approximation, we obtain the following for the inelastic wave function in the diffraction plane:

$$\Psi^{\alpha}_{n}(\mathbf{g},t) \approx -i\sigma_n \sum_{\mathbf{g}_1} \widetilde{W}^{\alpha}_{n0}(\mathbf{g}-\mathbf{g}_1,t-z_\alpha)\Psi_0(\mathbf{g}_1,z_\alpha), \tag{15}$$

which has the form of a single channeling expression, that is, a simple convolution, with the modified inelastic potential $\widetilde{W}^{\alpha}_{n0}$ replacing the true inelastic potential $\widetilde{V}^{\alpha}_{n0}$.

The results of this approximate double channeling model are presented for the 4 mrad detector in Figs. 3(a) and 3(d) and are seen to be in good agreement with the full double channeling calculations. For the larger detector sizes (25 and 60 mrad) in Fig. 3, the approximation given by Eq. (11) is too crude, and the results of the approximate model are not shown.

From Eq. (14) it is evident that in the special case of a small detector, a handle on the effects of double channeling can be obtained from our understanding of the way in which the quantity $S_{nn}(\mathbf{0},\mathbf{k},t-z)$ varies with depth z. This quantity can be interpreted as the complex conjugate of the wave function at depth z corresponding to a plane wave normally incident on the crystal *exit* surface (see, for instance, Ref. 55). During elastic scattering inside a simple crystal aligned along a major zone axis, electron density tends to accumulate at the sites of the atomic columns, producing "peaks" near the atomic columns and "troughs" between them. Consequently, the magnitude of the modified inelastic potential tends to be greater (less) than that of the true inelastic potential at positions near (between) the atomic columns. However, so far, we have made no mention of thermal absorption. This occurs only in the immediate vicinity of the atomic columns and therefore tends to counter the effects of elastic scattering by suppressing the amplitude of the wave function near the atomic columns to a degree depending on the atomic species in the column (and also, through the vibration amplitude, on the structure). All other things being equal, an atomic column of smaller atomic number causes less thermal absorption. This behavior is manifest in the results for the 4 mrad detector in Figs. 3(a) and 3(d): the signal generated by a probe directly positioned above a pure O column is enhanced by double channeling, as expected for the relatively weak thermal absorption from this column, whereas the greater thermal absorption from the considerably heavier Ti-O column (which contains the same number of O atoms as the pure O column) has countered any such enhancement. Furthermore, double channeling has suppressed the signal generated by a probe positioned between the pure O and Ti-O columns. Of course, it must be borne in mind that the extent to which this happens will depend on the scattering strength of the sample.

V. CONCLUSIONS

The elastic scattering of a fast incident electron prior and subsequent to an atomic ionization event in a crystal has implications for atomic resolution core-loss imaging in the STEM. Routine simulations incorporate elastic scattering prior to ionization (single channeling) but do not take into account elastic scattering subsequent to ionization (double channeling). For our case study, we considered O *K* loss images of $SrTiO_3$, and simulations were conducted for different specimen thicknesses and different detector sizes. We found that the degree to which single and double channeling results differ is mainly determined by the detector size. Perhaps unsurprisingly, for detector semiangles significantly smaller than the probe convergence semiangle, we found that double channeling can have a dramatic effect on the qualitative features of core-loss images. More surprisingly, significant qualitative differences between single and double channeling simulations persisted for a detector semiangle equal to the probe convergence semiangle (which was 25 mrad), even for thin specimens (about 100 Å). The presence of Ti atoms, enhancing the amount of elastic scattering, contributes to this result; simulations for the C *K* loss image of SiC, not presented here, show only minor differences when the detector semiangle is equal to the probe convergence semiangle. Nevertheless, for strongly scattering samples, our results suggest that the single channeling approximation may well be inadequate.

While feasible on current computers, double channeling calculations are computationally demanding. Simplified models, requiring significantly less computing time, are highly desirable. We have shown two limits in which the complication of a full double channeling calculation is not required. First, and already well known, for a detector semiangle that is significantly larger than the probe convergence semiangle, all inelastically scattered electrons are collected and so the single channeling approximation is valid (because it correctly predicts the total number of inelastically scattered electrons, though not their distribution). Second, for the case of a very small detector, an approximate double channeling model was introduced in which the computation time is essentially the same as the single channeling calculation. The validity domain of this model—very small detectors—is precisely that in which double channeling effects are strongest. However, both the approximate double channeling model and the single channeling approximation can fail for a detector semiangle matched to the probe convergence semiangle (which is an experimentally advantageous arrangement). At least presently, in such cases, we have no option but to resort to full double channeling calculations in order to gauge the validity of the single channeling approximation and, if it is invalid, to accurately compare to experimental data.

ACKNOWLEDGMENT

L.J.A. acknowledges support by the Australian Research Council.

---

*christian.dwyer@mcem.monash.edu.au

[1] H. Yoshioka, J. Phys. Soc. Jpn. **12**, 618 (1957).
[2] A. Howie, Proc. R. Soc. London, Ser. A **271**, 268 (1962).
[3] C. J. Humphreys and M. J. Whelan, Philos. Mag. **20**, 165 (1969).
[4] P. Rez, C. J. Humphreys, and M. J. Whelan, Philos. Mag. **35**, 81 (1977).
[5] C. J. Rossouw and M. J. Whelan, Ultramicroscopy **6**, 53 (1981).
[6] V. W. Maslen and C. J. Rossouw, Philos. Mag. A **49**, 735 (1984).
[7] Z. L. Wang, Acta Crystallogr., Sect. A: Found. Crystallogr. **45**, 636 (1989).
[8] W. Coene and D. V. Dyck, Ultramicroscopy **33**, 261 (1990).
[9] L. J. Allen, Ultramicroscopy **48**, 97 (1993).
[10] S. L. Dudarev, L. M. Peng, and M. J. Whelan, Phys. Rev. B **48**, 13408 (1993).
[11] C. Dinges, A. Berger, and H. Rose, Ultramicroscopy **60**, 49 (1995).
[12] T. W. Josefsson and L. J. Allen, Phys. Rev. B **53**, 2277 (1996).
[13] P. Stallknecht and H. Kohl, Ultramicroscopy **66**, 261 (1996).
[14] P. Schattschneider, M. Nelhiebel, M. Schenner, W. Grogger, and F. Hofer, J. Microsc. **183**, 18 (1996).
[15] K. Omoto, K. Tsuda, and M. Tanaka, J. Electron Microsc. **51**, 67 (2002).
[16] A. Fukuhara, J. Phys. Soc. Jpn. **21**, 2654 (1966).
[17] C. J. Rossouw and V. W. Maslen, Philos. Mag. A **49**, 743 (1984).
[18] C. J. Rossouw, Ultramicroscopy **16**, 241 (1985).
[19] Z. L. Wang, Acta Crystallogr., Sect. A: Found. Crystallogr. **48**, 674 (1992).
[20] P. Rez, Ultramicroscopy **52**, 260 (1993).
[21] L. J. Allen and T. W. Josefsson, Phys. Rev. B **52**, 3184 (1995).
[22] C. Dinges and H. Rose, Scanning Microsc. **11**, 277 (1997).
[23] C. Dwyer and J. S. Barnard, Phys. Rev. B **74**, 064106 (2006).
[24] E. J. Kirkland, Ultramicroscopy **102**, 199 (2005).
[25] D. K. Saldin and P. Rez, Philos. Mag. B **55**, 481 (1987).
[26] V. W. Maslen, Philos. Mag. B **55**, 491 (1987).
[27] C. Dwyer, Ultramicroscopy **104**, 141 (2005).
[28] J. D. Bjorken and S. D. Drell, *Relativistic Quantum Mechanics* (McGraw-Hill, New York, 1964).
[29] J. M. Cowley and A. F. Moodie, Acta Crystallogr. **10**, 609 (1957).
[30] P. Goodman and A. F. Moodie, Acta Crystallogr., Sect. A: Cryst. Phys., Diffr., Theor. Gen. Crystallogr. **30**, 280 (1974).
[31] L. Sturkey, Proc. Phys. Soc. London **80**, 321 (1962).
[32] C. J. Humphreys, Rep. Prog. Phys. **42**, 1825 (1979).
[33] P. G. Self, M. A. O'Keefe, H. R. Buseck, and A. E. C. Spargo, Ultramicroscopy **11**, 35 (1983).
[34] L. J. Allen, H. M. L. Faulkner, and H. Leeb, Acta Crystallogr., Sect. A: Found. Crystallogr. **56**, 119 (2000).
[35] A. Weickenmeier and H. Kohl, Philos. Mag. B **60**, 467 (1989).
[36] H. Kohl and H. Rose, Adv. Electron. Electron Phys. **65**, 173 (1985).
[37] D. A. Muller and J. Silcox, Ultramicroscopy **59**, 195 (1995).
[38] P. Schattschneider, M. Nelhiebel, H. Souchay, and B. Jouffrey, Micron **31**, 333 (2000).
[39] L. J. Allen, S. D. Findlay, M. P. Oxley, C. Witte, and N. J. Zaluzec, Phys. Rev. B **73**, 094104 (2006).
[40] S. D. Findlay, P. Schattschneider, and L. J. Allen, Ultramicroscopy **108**, 58 (2007).
[41] P. Schattschneider, M. Nelhiebel, and B. Jouffrey, Phys. Rev. B **59**, 10959 (1999).
[42] J. Verbeeck, D. V. Dyck, H. Lichte, P. Potapov, and P. Schattschneider, Ultramicroscopy **102**, 239 (2005).
[43] P. Schattschneider and W. S. M. Werner, J. Electron Spectrosc. Relat. Phenom. **143**, 83 (2005).
[44] H. Müller, H. Rose, and P. Schorsch, J. Microsc. **190**, 73 (1998).
[45] R. H. Ritchie and A. Howie, Philos. Mag. A **58**, 753 (1988).
[46] G. Anstis, Acta Crystallogr., Sect. A: Found. Crystallogr. **52**, 450 (1996).
[47] F. Herman and S. Skillman, *Atomic Structure Calculations* (Prentice-Hall, Englewood Cliffs, NJ, 1963).
[48] M. Bosman, V. J. Keast, J. L. García-Muñoz, A. J. D'Alfonso, S. D. Findlay, and L. J. Allen, Phys. Rev. Lett. **99**, 086102 (2007).
[49] K. Kimoto, T. Asaka, T. Nagai, M. Saito, Y. Matsui, and K. Ishizuka, Nature (London) **450**, 702 (2007).
[50] D. A. Muller, L. Fitting-Kourkoutis, M. Murfitt, J. H. Song, H. Y. Hwang, J. Silcox, N. Dellby, and O. L. Krivanek, Science **319**, 1073 (2008).
[51] L. J. Allen, S. D. Findlay, A. R. Lupini, M. P. Oxley, and S. J. Pennycook, Phys. Rev. Lett. **91**, 105503 (2003).
[52] E. C. Cosgriff, M. P. Oxley, L. J. Allen, and S. J. Pennycook, Ultramicroscopy **102**, 317 (2005).
[53] C. Dwyer, Phys. Rev. B **72**, 144102 (2005).
[54] A. J. D'Alfonso, S. D. Findlay, M. P. Oxley, and L. J. Allen, Ultramicroscopy (to be published).
[55] Y. Kainuma, Acta Crystallogr. **8**, 247 (1955).